Impact of Using Different Tissue Classes on the Accuracy of MR-based Attenuation Correction in PET-MRI

A. Akbarzadeh, M.R. Ay, *Member, IEEE* A. Ahmadian, *Senior Member, IEEE*
N. Riahi Alam and H. Zaidi, *Senior Member, IEEE*

***Abstract* – Diagnosis, staging and treatment of disease depends on the morphological and functional information obtained from multimodality molecular imaging systems. The combination of functional and morphological information is now routinely performed to overcome the limitations of each individual modality. Attenuation of photons in the object under study is one of the main limitations of quantitative PET imaging. Attenuation correction plays a pivotal role in PET imaging. However, the availability of CT data on hybrid PET/CT scanners made it possible to build an accurate attenuation map. One of the well-known methods for generation of the attenuation map on PE/MRI systems is MR-based attenuation correction (MRAC) where image segmentation is used to classify MRI into several classes corresponding to different attenuation factors. In this study we investigate the effect of using different numbers of classes for the generation of attenuation maps on the accuracy of attenuation correction of PET data. The study was carried out using simulations of the XCAT phantom and 10 clinical studies. For the later, CT and PET images of 10 patients were used with CT-based attenuation correction assumed as reference. MRI was classified into different classes to produce two, three and four-class attenuation maps using the ITK library. The relative error showed that the lower number of classes will increase the global error over 8%. The elimination of bony structures from the attenuation map will cause a local error over 3%. In clinical studies, $\mathbf{SUV_{mean}}$ and $\boldsymbol{SUV_{max}}$ were calculated for each AC method. The results seem to indicate an underestimation of 11% because of neglecting bone.**

Manuscript received November 4, 2011. This work was supported by Tehran University of Medical Sciences under grant No. 10934 and the Swiss National Science Foundation under grant No. 31003A-125246.

A. Akbarzadeh is with Research Center for Science and Technology in Medicine, Tehran University of Medical Sciences, Tehran, Iran as well as Department of Medical Physics and Biomedical Engineering, Tehran University of Medical Sciences

M.R. Ay is with Department of Medical Physics and Biomedical Engineering, Tehran University of Medical Sciences, Tehran, Iran. He is with with Research Center for Science and Technology in Medicine, Tehran University of Medical Sciences, Tehran, Iran as well as Research Institute for Nuclear Medicine, Tehran University of Medical Sciences, Tehran, Iran. (e-mail: mohammadreza_ay@sina.tums.ac.ir).

A. Ahmadian is with Research Center for Science and Technology in Medicine, Tehran University of Medical Sciences, Tehran, Iran as well as Department of Medical Physics and Biomedical Engineering, Tehran University of Medical Sciences

N. Riahi Alam is with Department of Medical Physics and Biomedical Engineering, Tehran University of Medical Sciences

H. Zaidi is with Geneva University Hospital, Division of Nuclear Medicine and Molecular Imaging, Geneva, Switzerland and the Department of Nuclear Medicine and Molecular Imaging, University Medical Center Groningen, Groningen, Netherlands (e-mail: habib.zaidi@hcuge.ch).

I. Introduction

Clinical diagnosis, staging, and patient treatment mostly rely on morphological and molecular imaging procedures such as magnetic resonance imaging (MRI), computed tomography (CT), and positron emission tomography (PET). There are, however, prominent constraints to radiological and functional imaging studies, which deteriorate their diagnostic accuracy in assessing tumor stages or therapy response [1, 2]. It has been reported that the morphological information is complementary to functional imaging. Multimodality imaging suggests the combination of morphological information on the tumor and potential metastases (which is provided by CT or MR) with functional data on tumor metabolism (provided by PET) [3, 4]. PET/MR and PET/CT are two bywords of multimodality imaging systems which combine the morphological information of the MRI or CT with the metabolic information of PET. The main challenge of quantitative PET imaging is the attenuation of annihilated photons on the object under study. The mere solution for this issue is to find the attenuation map of object under study for the purpose of attenuation correction. In PET/CT systems the attenuation is generated easily using the CT image [5]. The CT image contains all intensities in HU which can be converted to the attenuation factor in 511 keV for PET attenuation correction using different methods[6] . However, in PET/MR systems the story is completely different. Since MRI signal is not associated with attenuation factor at all, the direct generation of attenuation map from MRI image is impossible. Nevertheless there are handful indirect methods to produce attenuation map from MRI image [7].

There are different strategies for generation of attenuation map at 511 keV from MR images. One category of these methods rely on a reference atlas to determine the attenuation map by registering the standard attenuation map from atlas on MR image of current patient. The others use a segmentation method to identify the organs, then assign attenuation factor to each individual organ [8]. This method is more general and not only is employed in MRAC techniques but also CTAC methods take the advantage of tissue classification[5]. The noticeable question about the MRAC is, which organs are appropriate to be segmented and consequently to be considered in attenuation map. The most tragic fact here is that some organs like chest and vertebral bones are not distinguishable in whole body MRI images. Some studies proposed the ignorance of bones [8] and even some groups

used the attenuation map containing 2 classes of soft tissue and lungs [9].

The dubious issue of neglecting bone in the attenuation map prompts further questions about the accuracy of quantitative PET studies that use boneless attenuation map for attenuation correction. To be clearer, the relationship between the number of classes in the attenuation map and the resulting error is a matter of curiosity. Although it is obvious that different classes of intensity will result in different activity values, the optimal number of classes (with the least misclassification error) is still unknown.

In this study, we quantitatively evaluated the influence of using different tissue classes on the accuracy of MRAC of PET data based on simulation using both the XCAT model and clinical studies.

II. Materials and Methods

A. XCAT phantom simulations

The XCAT phantom was used to simulate 3D activity and attenuation maps of the human anatomy. The XCAT (4D extended cardiac-torso) phantom [10, 11] was developed for realistic simulation of human anatomy and physiology for nuclear medicine studies. This phantom is a kind of database that gets an input file containing the phantom information such as anatomic height, weight, gender and the amount of activity for each organ then creates two sets of 3D images: (a) activity map based on list of activities in the input file and (b) the corresponding attenuation map for 511 keV.

Fig. 1 summarizes The flowchart of phantom study, however different steps explained in more detail as follow:

1. A male phantom (a 3D activity image of PET) along with its correspondent attenuation map in 511 keV was generated. The assigned activity for each region was calculated using a combination of available patient's PET data and raylman's study [12]. The size of phantom was considered to be 256 × 256 × 921containing voxels of size 2×2×2 mm^3.
2. In order to assess the effect of different classification of attenuation map, the attenuation map was segmented into two, three and four classes. The threshold and assigned value is reported in table 1.
3. In order to analytically produce PET raw data the original and ideal activity map (obtained in stage 1) is attenuated using generated attenuation map by XCAT at 511 keV. (The STIR software holds an option to undo attenuation which is inverse of the well-known attenuation correction algorithm)
4. The attenuated emission sinogram resulted from former stage, is corrected for attenuation using the 4 different attenuation maps (2-Calss, 3-Class, 4-Class and gold-standard) which were achieved in stage 2.
5. The corrected image is compared with the original activity image and the relative error was calculated.

A. Patient based simulation:

The motivation behind our further assessment on simulation based on patient data was evaluation of our strategy in more complex and actual situation.

For patient data assessment we took the advantage of F-FDG PET/CT whole body images. Images of 10 patients were obtained using Biograph 16 PET/CT scanner (Siemens Medical Solutions, Erlangen, Germany). PET images were acquired with a slice thickness of 5 mm and pixel size of 4.0728×4.0728 mm^2 and dimensions of 168×168×300-400. In order to perform CT based attenuation correction a low-dose CT scan were done on CT module of PET/CT system.

The reconstruction process along with all corrections was carried out on the system to achieve all PET images which quantify the activity concentration in Bq/ml.

The process of patient data assessment is identical to aforementioned phantom assessment (5 stages), but with two extra steps (see Fig. 1 gray dashed cubes):

TABLE I. Thresholds for segmentation of the attenuation map into different classes and the assigned value. Using the pattern: LOWER THR < I < UPPER THR ← ASSIGNED VALUE

	Class1	Class2	Class3	Class4
Two-class map	I<0.096←0.0286	0.096<I←0.096	–	–
Three-class map	I<0.096←0.0286	0.096<I<0.134←0.096	0.134<I←0.134	–
Four-class map	I<0.096←0.0286	0.096<I<0.101←0.096	0.101<I<0.134←0.0101	0.134<I←0.134

TABLE II. HU thresholds for segmentation of CT image into different classes as well as assigned value. Using the pattern: LOWER HU < I < UPPER HU ← ASSIGNED VALUE

	Class1	Class2	Class3	Class4
Two-class map	I<-200←0.0286	-200<I←0.096	–	–
Three-class map	I<-200←0.0286	-200<I<300←0.096	300<I←0.134	–
Four-class map	I<-200←0.0286	-200<I<100←0.096	100<I<300←0.0101	300<I←0.134

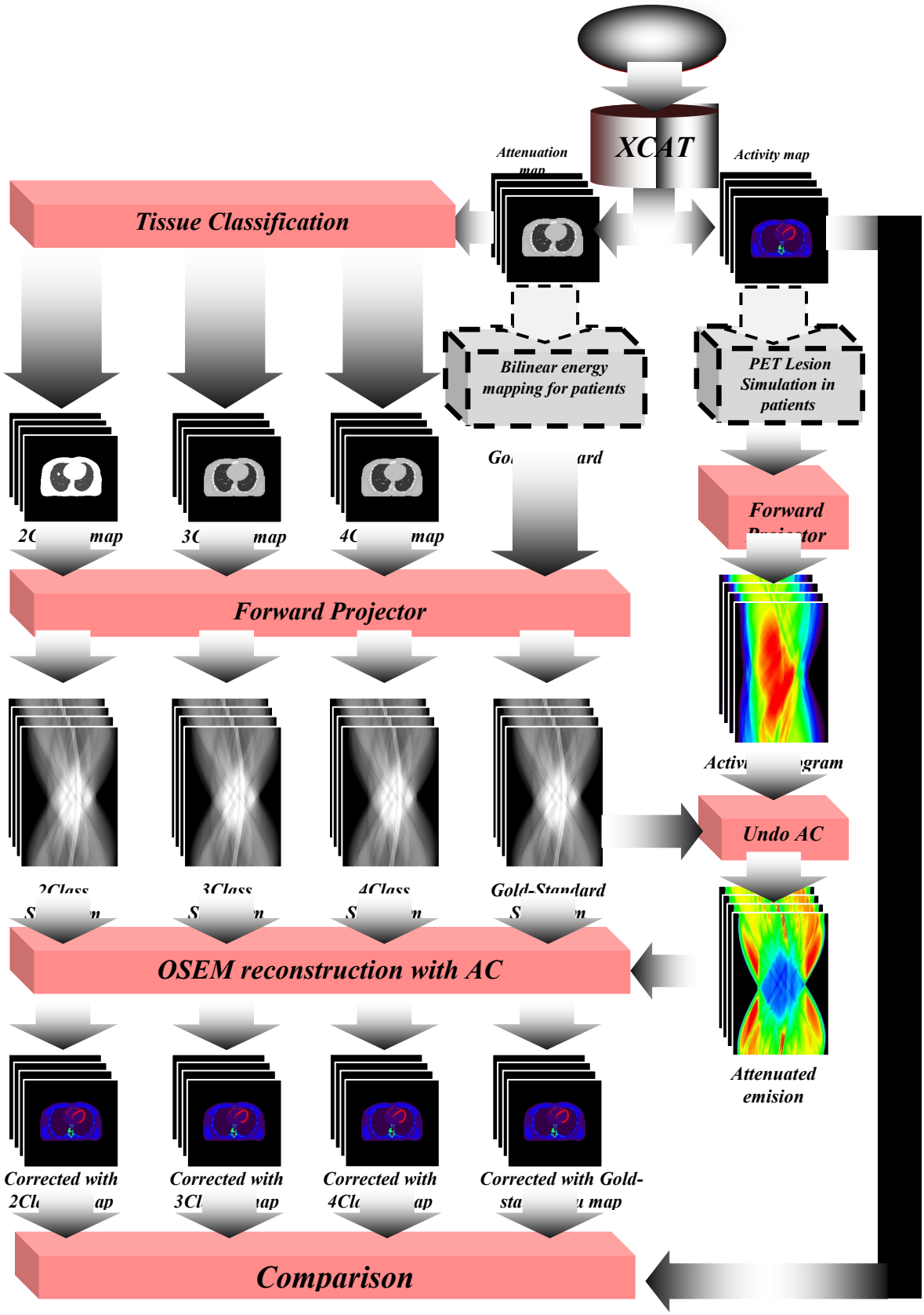

FIG. 1. Flowchart of the overall procedure followed for assessment of simulated and clinical studies.

(a) bilinear energy mapping method was used to generate the attenuation map from patients' CT images in order to use in STIR reconstruction software. It should be noted that the emission raw data sinograms of patient generated using STIR software and the original raw data provided by scanner was not used due to the fact it was not possible to reconstruct them using STIR as it needs several sensitivity calibration files from the scanner. (b) Implementation of several virtual lesions with different SUVs to assess the effect of different classes of attenuation maps on the clinical interpretation.

The step (a) was fulfilled using the famous bilinear energy mapping algorithm on CT images. For step (b), clinical experts suggested manually creating lesions inside the bones to imitate the sizes and activities of osteo-metastatic tumors. The lesions were randomly located inside the bone areas in random radiuses of 1-4 cm and with SUV of 2.5.

Similar to phantom assessment the CT image is segmented

To produce 2-class, 3-class and 4-class attenuation maps (Table 2). 2-class attenuation map which ignores the bone and consists of lungs and soft tissue is like what is being used in MR based attenuation correction. The 3-Class considers the both spongy bones and hard bones inside a new class in addition to previous two classes. On the other hand the 4-Class attenuation map separates the soft bones and hard bones in two separate classes.

B. Segmentation and reconstruction tools

All the segmentation processes were done using ITK object oriented image processing library written in C++ [13]. The reconstruction carried out using the well known OSEM method with 8 subsets and 4 iterations. All of the attenuation correction and reconstruction was done using STIR library[14].

C. Comparison and error analysis

For phantom study the relative error of reconstructed images was calculated voxel by voxel subtracting the result image from the activity data, dividing into activity data (1).

$$\text{Relative Error} = \frac{original\ activity\ data - corrected\ data}{original\ activity\ data} \times 100\% \quad (1)$$

Likewise for the patient study the attenuation correction and reconstruction procedures were done using the STIR library. The spherical ROIs surrounding all lesions were located in places and the standard uptake value (SUV) was calculated for each ROI[15].. We calculated the SUV over an ROI using the formula below:

$$\text{SUV}_{\text{mean/max}} = \frac{The\ mean/\max activity\ concentration\ in\ ROI}{Injected\ Dose/\ body\ weight} \quad (2)$$

The $\text{Error}_{\text{mean/max}}$ which directly shows the dispersion of the $\text{SUV}_{\text{mean/max}}$ from the original SUV of the PET images, is calculated by the following formula:

$$\text{Error}_{\text{mean/max}} = \frac{SUV_{mean/max} - Original\ SUV}{Original\ SUV} \quad (3)$$

III. Results

Fig. 2 shows the error map (image that contains the amount of relative error) whose voxel values indicate the percentage of relative errors (equation 1).

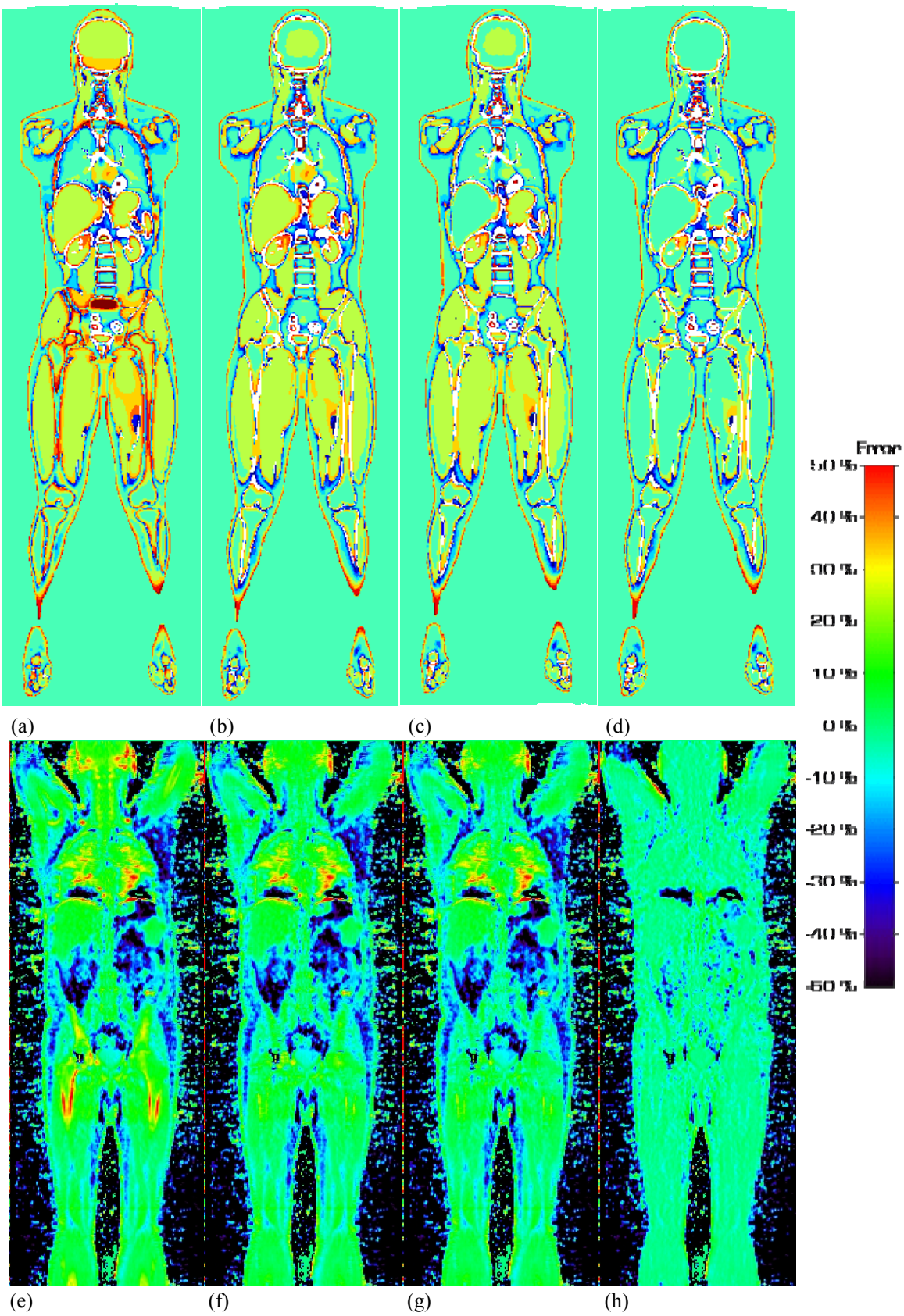

Fig. 1. Calculated error maps resulting from AC of phantom (a-d) and patient (e-h) data. The AC is based on: (a,e) two-class attenuation map (b,f) three-class attenuation map (c,g) four-class attenuation map (d,h) gold-standard attenuation map

Fig. 3 shows the error map statistical population which can be considered as the histogram of error map. The vertical axes of the histogram shows the count of voxels that hold the same errors.

The top located histogram has counted all voxels of the image and the bottom located histogram has counted just bone areas.

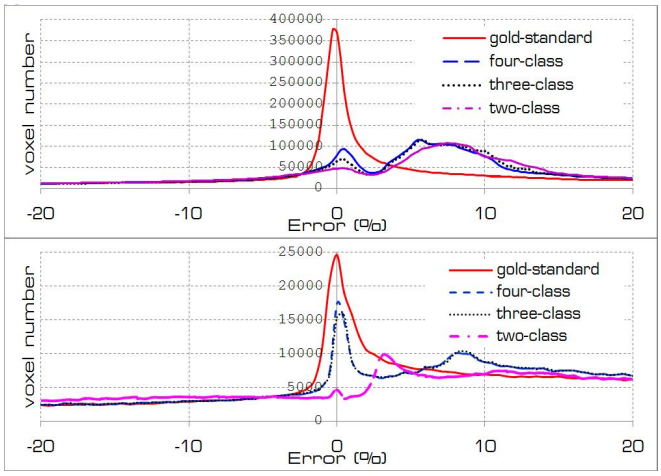

Fig. 2. Histogram of error images (top) global histogram (bottom), bony structures and their neighborhood.

The results of evaluations for patient study are indicated using box and whisker plot. The box shows the median (red horizontal line) and the lower (Q1) and upper quartiles (Q3) (defined as the 25th and 75th percentiles). The red colored plus sign in the plots indicates the outliers. Outliers in our plot include the dubious results which are beyond of 1.5 times Interqurtile range (Q3-Q1). The whiskers show the maximum and minimum of population after elimination of outliers.

Fig. 4 shows box and whisker plots for SUVs that were calculated in all 203 ROIs in 10 patients. The original value is the created SUV values in all ROIs.. As Fig. 4 (a) shows the CT based attenuation correction causes 6.8% overestimation in SUV_{max} However the attenuation correction method based on 3-class and 4-calls classified attenuation map shows smaller error value.

Fig. 4 (b) reports the overall underestimation SUV_{mean} either of CT based attenuation map or classified attenuation maps. This problem originates from the inherent numerical instability of iterative reconstruction algorithm. Nevertheless, increasing the number of classes in the attenuation map will decrease the estimated error and improves the results.

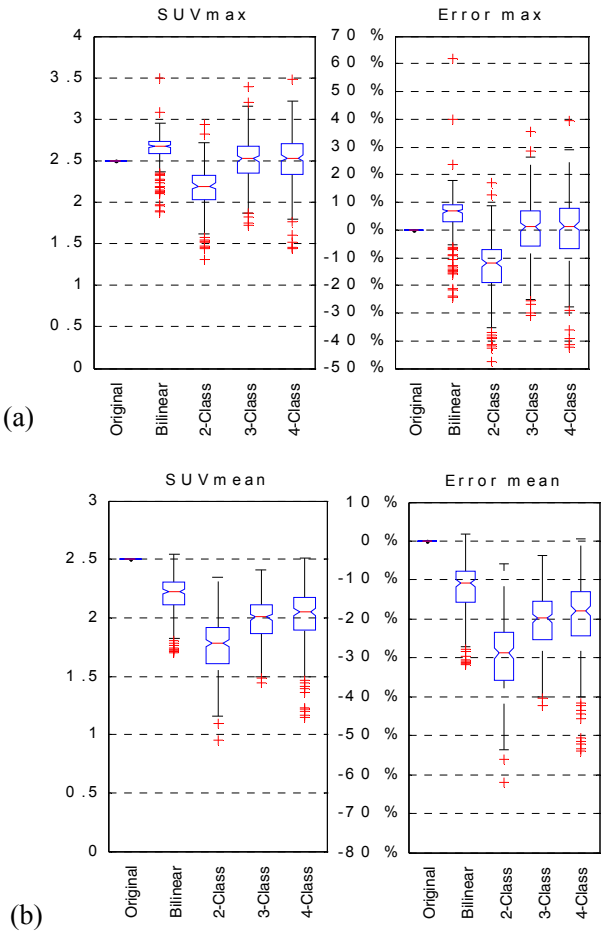

Fig. 3. box and whisker plots along with relative error percentage which calculated for different AC methods. (a) SUV_{max} and its relative error (b) SUV_{mean} and its relative error.

IV. Discussion:

The phantom simulation study substantiates the fact that the lower the number of classes in attenuating map the more the resulting recovery activity deviates from the original activity. Masking the background of error images, their histogram was plotted which shows the global effect (effect in whole body). The second histogram was obtained by merely in bones and their neighborhood to evaluate the local deterioration caused by malfunction of attenuation correction procedure. As Fig. 3-top shows using the gold standard attenuation map for AC the majority of voxels hold an error value around zero. Using four-class attenuation map there are two peaks in histogram. The population of voxels with zero error decreased and there is second peak in 5.5% which indicates that a part of data was underestimated. The population of zero intensity voxels is reduces as the number of classes goes down and the second peak shifts to the right, 5.75% for three-class and 7.5% for two-class. It is obvious that four-class and three-class that considered the bone in the attenuation map, behave identically. Around bony structures the attenuation correction

based on two-class shows a drastic decrease in population of zero error voxels with underestimation over 3%.

The patient simulation study shown in Fig. 3 (b) reports that the SUV_{mean} calculated over 203 ROIs of 10 patients, and supports the notion that higher number of classes will improve the accuracy of PET data. This notion is in harmony with the previously mentioned phantom study. However, the results from SUV_{max} indicate an error of 1-2 % for 4-class and 3-class attenuation maps which is better than the bilinear attenuation map. Fig. 3 (a). The single maximum voxel value inside the ROI is chosen to measure the SUV_{max} , because it is less dependent on the shape, size and location of ROI. Notwithstanding this philosophy, the SUV_{max} suffers from the worse reproducibility in comparison with $\mathrm{SUV_{mean}}$ [16]. Thus in our study SUV_{mean} is more reliable owing to the fact that the ROIs were drawn by automatically by computer and there is no error in size and locations of ROIs.

Considering bones in the attenuation map improves the relative $\mathrm{Error_{mean}}$ by around 11% (compare 2-class and 3-class). The proposed segmentation method for MR based attenuation correction by Moller[8] has alleged that the bone ignorance will cause small differences from CT based attenuation map (<8%). Our results on the contrary, show that the ignorance of bone will cause 28% underestimation in SUV_{mean}. Hofmann et.al[17] in their recent study showed bone ignorance in attenuation map will cause relative error above 10%, in 38% of their located ROIs inside the bone areas. Our results are in good agreement with this study which prohibited the quantification tasks when bones are ignored in attenuation maps.

V. Conclusion:

We quantified the effect of using different number of classes in segmentation based attenuation correction in PET-MRI. The motivation behind our study was the controversial issue of neglecting bone in the segmentation based approach for PET/MRI systems. Overall, the results show the efficacy of increasing the number of classes on the accuracy of attenuation correction in PET. The clinical studies substantiates that the number of classes will cause a significant effect on the clinical interpretation of the osteo-metastatic lesions. Moreover, considering bony structures in the attenuation map will improve the accuracy of MR-based attenuation correction.

References

[1] G. P. Schmidt, *et al.*, "[Whole-body MRI and PET/CT in tumor diagnosis.]," *Radiologe,* vol. 44, pp. 1079-87, Nov 2004.

[2] M. D. Seemann, *et al.*, "Assessment of the extent of metastases of gastrointestinal carcinoid tumors using whole-body PET, CT, MRI, PET/CT and PET/MRI," *Eur J Med Res,* vol. 11, pp. 58-65, Feb 21 2006.

[3] W. D. Heiss, "The potential of PET/MR for brain imaging," *Eur J Nucl Med Mol Imaging,* vol. 36 Suppl 1, pp. S105-12, Mar 2009.

[4] G. Antoch and A. Bockisch, "Combined PET/MRI: a new dimension in whole-body oncology imaging?," *Eur J Nucl Med Mol Imaging,* vol. 36 Suppl 1, pp. S113-20, Mar 2009.

[5] P. E. Kinahan, *et al.*, "X-ray-based attenuation correction for positron emission tomography/computed tomography scanners," *Semin Nucl Med.,* vol. 33, pp. 166-79., 2003.

[6] M. R. Ay, *et al.*, "Comparative assessment of energy-mapping approaches in CT-based attenuation correction for PET," *Mol Imaging Biol,* vol. 13, pp. 187-98, Feb 2011.

[7] H. Zaidi and A. D. Guerra, "An outlook on future design of hybrid PET/MRI systems," *Med Phys,* vol. 38, p. 5667-5589, Oct 2011.

[8] A. Martinez-Moller, *et al.*, "Tissue classification as a potential approach for attenuation correction in whole-body PET/MRI: evaluation with PET/CT data," *J Nucl Med,* vol. 50, pp. 520-6, Apr 2009.

[9] V. Schulz, *et al.*, "Automatic, three-segment, MR-based attenuation correction for whole-body PET/MR data," *Eur J Nucl Med Mol Imaging,* vol. 38, pp. 138-52, Jan 2011.

[10] W. P. Segars, *et al.*, "Realistic CT simulation using the 4D XCAT phantom," *Med Phys,* vol. 35, pp. 3800-8, Aug 2008.

[11] W. P. Segars, *et al.*, "4D XCAT phantom for multimodality imaging research," *Med Phys,* vol. 37, pp. 4902-15, Sep 2010.

[12] R. R. Raylman, *et al.*, "Capabilities of two- and three-dimensional FDG-PET for detecting small lesions and lymph nodes in the upper torso: a dynamic phantom study," *Eur J Nucl Med,* vol. 26, pp. 39-45, Jan 1999.

[13] T. S. Yoo, *et al.*, "Engineering and algorithm design for an image processing Api: a technical report on ITK--the Insight Toolkit," *Stud Health Technol Inform,* vol. 85, pp. 586-92, 2002.

[14] K. Thielemans, *et al.*, "STIR: Software for Tomographic Image Reconstruction Release 2," in *Nuclear Science Symposium Conference Record, 2006. IEEE*, San Diego, CA, USA, 2006, pp. 2174-2176.

[15] J. A. Thie, "Understanding the standardized uptake value, its methods, and implications for usage," *J Nucl Med,* vol. 45, pp. 1431-4, Sep 2004.

[16] C. Nahmias and L. M. Wahl, "Reproducibility of standardized uptake value measurements determined by 18F-FDG PET in malignant tumors," *J Nucl Med,* vol. 49, pp. 1804-8, Nov 2008.

[17] M. Hofmann, *et al.*, "MRI-Based Attenuation Correction for Whole-Body PET/MRI: Quantitative Evaluation of Segmentation- and Atlas-Based Methods," *J Nucl Med,* vol. 52, pp. 1392-9, Sep 2011.